Access to this work was provided by the University of Maryland, Baltimore County (UMBC) ScholarWorks@UMBC digital repository on the Maryland Shared Open Access (MD-SOAR) platform.

Please provide feedback

Please support the ScholarWorks@UMBC repository by emailing scholarworks-group@umbc.edu and telling us what having access to this work means to you and why it's important to you. Thank you.

Correspondence to:
G. Q. Yan,
gqyan@spaceweather.ac.cn

Substructure of a Kelvin-Helmholtz Vortex Accompanied by Plasma Transport Under the Northward Interplanetary Magnetic Field

G. Q. Yan[1], **F. S. Mozer[2]**, **G. K. Parks[2]**, **C. L. Cai[1]**, **T. Chen[1]**, **M. L. Goldstein[3]**, and **Y. Ren[1]**

[1]State Key Laboratory of Space Weather, National Space Science Center, Chinese Academy of Sciences, Beijing, China, [2]Space Science Laboratory, University of California, Berkeley, CA, USA, [3]University of Maryland Baltimore County, Baltimore, MD, USA

Abstract Within a Kelvin-Helmholtz (K-H) vortex at the duskside magnetopause, a substructure characterized by two flux enhancements of cold magnetosheath plasma in a background of hot magnetosphere plasma is observed. The substructure is accompanied by plasma transport across the magnetopause, and the transport region is found to split into two parts: the double peaks in both ion and electron densities, corresponding to the two flux enhancements in spectrograms. There are two decreases in the ion temperature while the electron temperature remains constantly low, suggesting that the substructure is caused by a secondary process within the vortex rather than the secondary crossings of the vortex or the boundary oscillations. A transverse motion of cold plasma is observed in the pitch-angle distribution, demonstrating an example of transverse driving and ongoing plasma transport across the magnetopause. With the convective electric field removed, the perturbed electric field E_1, which is sinusoidal and perpendicular to B, matches the theoretical prediction of the Rayleigh-Taylor (R-T) instability. Such a perturbed electric field is expected to be the electrostatic field that accompanies the R-T instability producing the substructure and drives the plasma transport by $E_1 \times B$ drift. The observations suggest that this secondary R-T instability within the K-H vortex can drive plasma transport across the magnetopause.

Plain Language Summary The Earth's intrinsic magnetic field creates a bubble called the magnetosphere which protects the planet from direct bombardment by the solar wind. The outer edge of the magnetosphere, the magnetopause, prevents the direct incursion of solar wind plasma into the magnetosphere. Sometimes, the solar wind can penetrate into the magnetosphere by changing the topology of the magnetopause via a process known as magnetic reconnection. In addition, transport can proceed via the Kelvin-Helmholtz (K-H) instability which creates vortices, the ripples on the flanks of the magnetopause, as shown in some numerical simulations (Matsumoto & Hoshino, 2004, 2006; https://doi.org/10.1029/2003gl018195, https://doi.org/10.1029/2004ja010988). Here, based on spacecraft observations thousands of miles away, we show a secondary structure of the plasma transport across the magnetopause within a K-H vortex. The observations of both plasma and electric fields have revealed detailed microphysics of plasma transfer within the ripples at the magnetopause.

1. Introduction

The Kelvin-Helmholtz (K-H) instability is a macroscopic instability that can cause displacement of an interface between two different plasma regions separated by a velocity shear (Chandrasekhar, 1961). Driven by velocity shear at the magnetopause, the K-H instability has been observed to propagate tailward as surface waves in its linear stage and form vortices in the fully nonlinear stage. A statistical survey (Kavosi & Raeder, 2015) indicates that the K-H waves are ubiquitous at the magnetopause under many kinds of interplanetary magnetic field (IMF) conditions. Many observations of K-H waves have been reported (Chen & Kivelson, 1993; Chen et al., 1993; Kivelson & Chen, 1995; Hasegawa et al., 2004; Nykyri et al., 2006; Hwang et al., 2011, 2012; Yan et al., 2014; Farrugia et al., 2014; Walsh et al., 2015; Grygorov et al., 2016; Adamson et al., 2016; Ma et al., 2016; Lu et al., 2019). In addition, numerous magnetohydrodynamic (MHD) simulations have focused particular emphasis on the activation of the K-H instability (Miura, 1987, 1992, 1995; Hashimoto & Fujimoto, 2005), its evolution (Takagi et al., 2006), self-organization (Miura, 1999a, 1999b), and global distribution (Guo et al., 2010; Li et al., 2012), as well as its interaction with reconnection (Nykyri & Otto, 2001; Otto & Fairfield, 2000). The

Writing – original draft: G. Q. Yan
Writing – review & editing: F. S. Mozer, G. K. Parks, C. L. Cai, T. Chen, M. L. Goldstein, Y. Ren

magnetic reconnection at the magnetopause is the main mechanism to transport solar wind into the magnetosphere (Dai, 2009, 2018; Dai et al., 2017; Dungey, 1961; Song & Russell, 1992). The K-H instability and associated secondary processes can transport solar wind plasma into the magnetosphere (Faganello & Califano, 2017; Johnson et al., 2014; Masson & Nykyri, 2018; Welling et al., 2015). These processes within K-H vortices include: the magnetic reconnection when the magnetic field on both sides of the interface are parallel (Ma et al., 2017; Nykyri et al., 2006; Nykyri & Otto, 2001), the diffusive processes via turbulence where varieties of secondary processes such as secondary K-H or R-T instabilities are activated (Cowee et al., 2009; Matsumoto & Hoshino, 2004; Nakamura et al., 2004), or the conversion from K-H waves to kinetic Alfvén waves (KAWs) where the anomalous transport can occur (Chaston et al., 2007; Johnson & Cheng, 1997). Magnetic islands with large-area and higher plasma density can be detached into the magnetosphere in the reconnection process within K-H vortices, forming the blobby transport with the mass diffusion coefficient of 1×10^9 m^2 s^{-1} (Nykyri & Otto, 2001). In a 3D simulation model, the mid-latitude reconnections near the shear flow produce effective plasma transport with the mass diffusion coefficient of 1×10^{10} m^2 s^{-1} (Ma et al., 2017). MHD Simulations including the Hall-term in the generalized Ohm's law show that both the plasma transport driven by reconnection within K-H vortices and the transport driven by the secondary K-H or R-T instabilities can occur simultaneously (Nykyri & Otto, 2004). The blobby transport and diffusive transport are quantified by using both Hall-MHD with test particles and hybrid simulations (Ma et al., 2019), resulting in similar particle mixing rates. Comparison shows that the plasma is mainly transported through big magnetic islands produced by the reconnection within K-H vortices in Hall-MHD simulation, while the magnetic islands are small and patchy in hybrid simulation.

Along the magnetopause deformed by the K-H vortex, secondary K-H vortices can be further activated by velocity shear at the boundary. In an MHD simulation that includes finite electron inertia, a secondary K-H instability was found to cause decay of the parent K-H vortex and consequent mixing of the plasmas from both sides of the shear layer (Nakamura et al., 2004). The R-T instability is also a macroscopic instability when gravity exists in the opposite direction to the density gradient at the boundary between two fluid entities. It can arise at the magnetopause where the centrifugal force or other inertial force plays the role of gravity, and the density gradient opposite to the centrifugal force supplies the growth rate by making the complex frequency in the dispersion relation

$$\omega^2 - k u_0 \omega - \frac{g_c}{n_0}\frac{\partial n_0}{x} = 0 \tag{1}$$

For the R-T instability, the centrifugal force drives the charge dependent $\boldsymbol{g}_c \times \boldsymbol{B}$ drift along the boundary, resulting in charge separation because ions and electrons drift in opposite directions and in a speed proportional to the mass. In turn, the perturbed electric field $\boldsymbol{E}_1$ due to the charge separation gives rise to growing amplitudes via $\boldsymbol{E}_1 \times \boldsymbol{B}$ drift once any small disturbance is introduced, as illustrated in panel 1 of Figure 1. The charge separation electric field $\boldsymbol{E}_1$ is the solution of Poisson equation. With the typical sinusoidal perturbations along the surface, the solution should follow the sinusoidal forms

$$E_{1x} = \frac{4\pi\sigma}{\varepsilon}\cos(ky)e^{-kx}$$
$$E_{1y} = \frac{4\pi\sigma}{\varepsilon}\sin(ky)e^{-kx} \tag{2}$$

where σ is the surface charge density on the boundary. Both components of the electrostatic field sinusoidally vary along the y direction and exponentially decline along the x direction (x is confined to the boundary layer containing density gradient), with a phase difference of 90° between them (Rosenbluth & Longmire, 1957). It was discovered in a full particle simulation of the K-H instability at a density interface that a secondary R-T instability played a crucial role in the collapse of the K-H vortices resulting in turbulence and mass transport from the dense region to the tenuous region (Matsumoto & Hoshino, 2004, 2006). Small scale ripples of ion inertial scale have been also found in Hall-MHD simulations under northward IMF condition (Nykyri & Otto, 2004). However, such secondary processes in combination with the K-H instability that cause plasma transport have been found only in numerical simulations. Such secondary processes have, as yet, not been observed by spacecraft at the magnetopause.

Observational evidence of such secondary processes would provide important clues to the microphysics of the plasma transport across the magnetopause via K-H vortices. In recent observations, more details of smaller scale processes have been revealed. Plasma transport within K-H vortices has been discussed in some observations
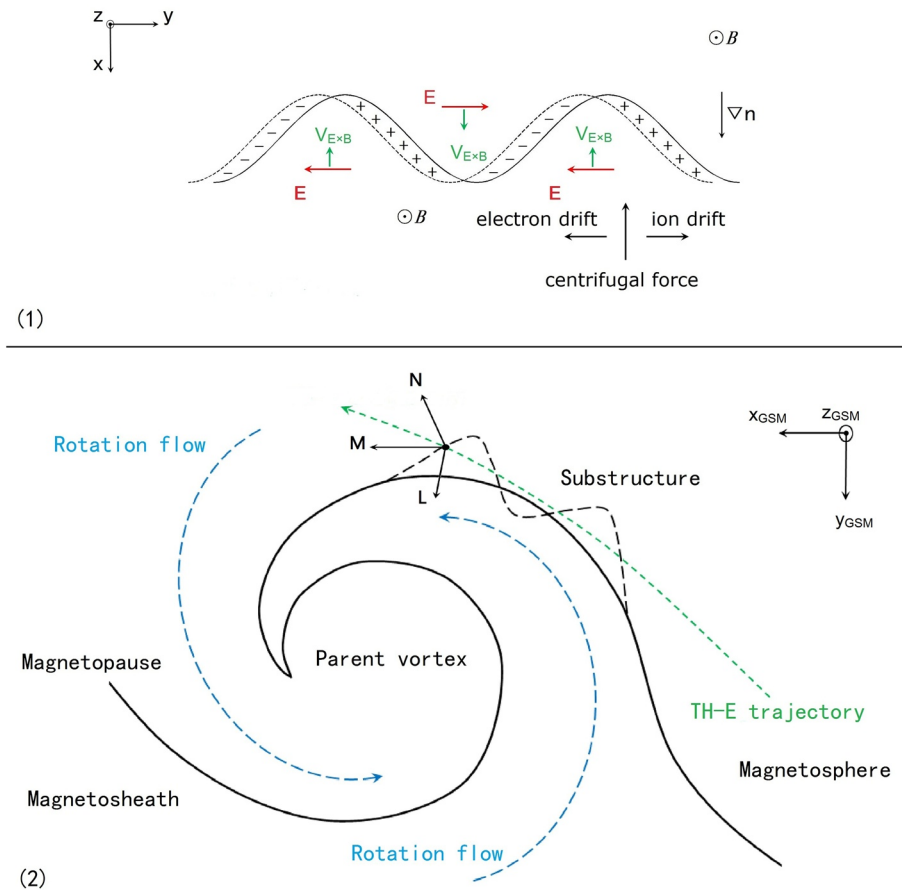
Figure 1. Illustrations of (1) the R-T instability and (2) the substructure formed by the secondary R-T instability process. Note that the XYZ coordinates are used to describe the R-T instability in panel 1 and the GSM coordinates are used to view the substructure of the vortex from northward of Z in panel 2.

(Fujimoto et al., 2003; Hasegawa et al., 2004; Sckopke et al., 1981). There are also many studies that have addressed plasma transport processes within K-H vortices, such as KAWs (Chaston et al., 2007) and vortex induced reconnection (Eriksson et al., 2016; Nakamura, Eriksson, et al., 2017; Nakamura, Hasegawa et al., 2017). In the K-H vortices observed by Cluster at the dawnside magnetopause, a kinetic magnetosonic wave was found to heat the cold plasma originating from the magnetosheath (Moore et al., 2016). Such an innovative mechanism is valuable for the interpretation of plasma heating in the universe, but their discussions focused on energy transport. Following the previous work, we present here Time History of Events and Macroscale Interactions during Substorms (THEMIS) observations of a substructure of a parent K-H vortex accompanied by plasma transport across the magnetopause, as illustrated in panel 2 of Figure 1. The transverse motion of the cold plasmas driven by $E_1 \times B$ drift is observed, indicating ongoing plasma transport in the substructure moving from the magnetosheath into the magnetosphere. The perturbed sinusoidal electric field was detected, as theoretically predicted by Equation 2. That electric field accompanies the generation of the substructure via the R-T instability.

2. Observations

We use measurements from the electrostatic analyzer (ESA; McFadden et al., 2008), fluxgate magnetometer (FGM; Auster et al., 2008), and electric field instrument (EFI; Bonnell et al., 2008) on board THEMIS-E (Angelopoulos, 2008) to investigate the details of an event. THEMIS-B at the lunar orbit supplies the IMF conditions. The time resolutions of the plasma parameters such as the velocity, temperature, density and the electric and magnetic fields are 3 s, while the magnetic field data have the time resolution of 1/16 s. ESA supplies ion and
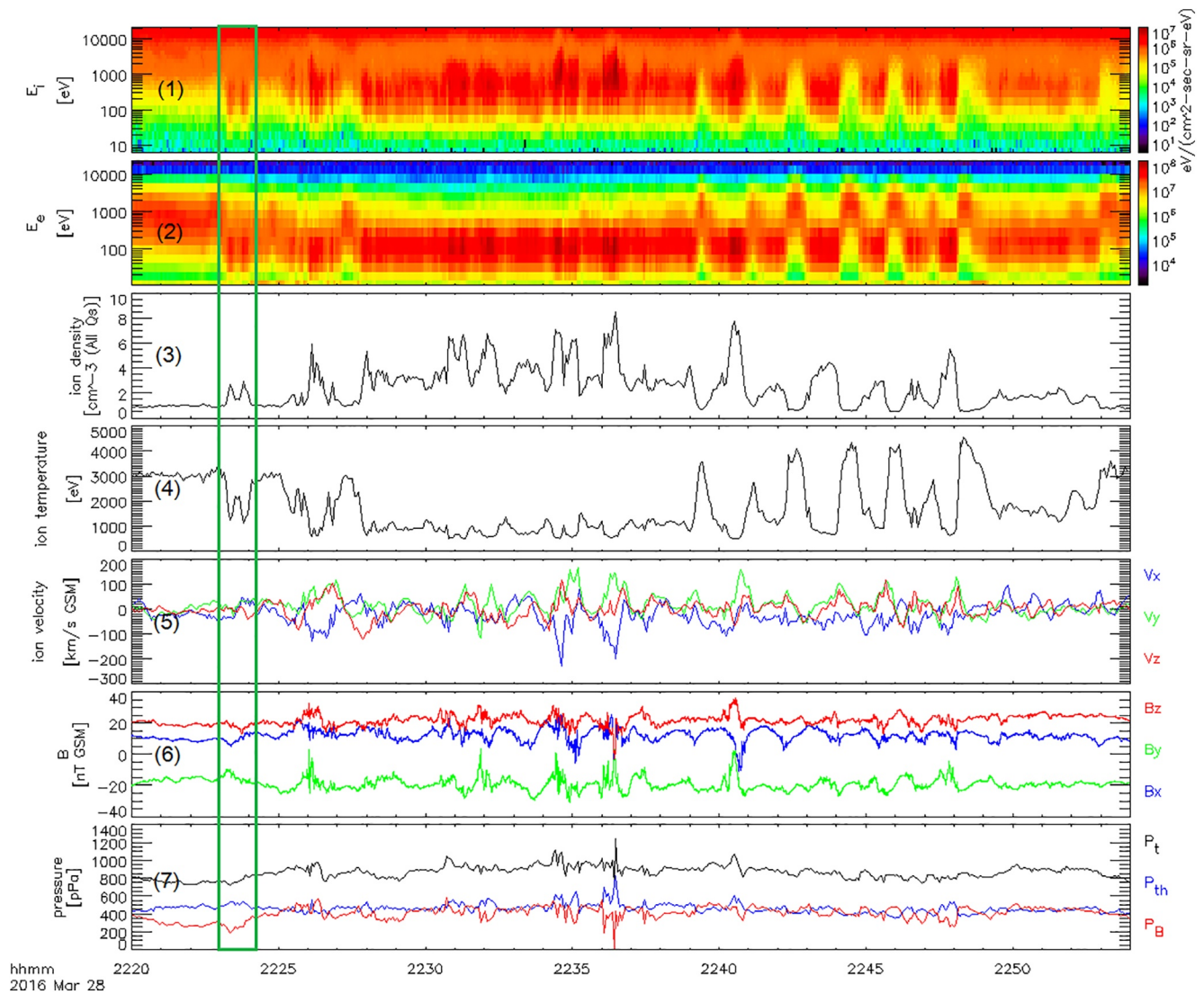
Figure 2. Overview of the vortex train observed by THEMIS-E. Panels 1 and 2 show the ion and electron spectrograms, respectively. Panels 3 and 4 show the ion density and temperature, respectively. Panel 5 gives the ion bulk velocity components in GSM coordinates. Panel 6 gives the magnetic field components in GSM coordinates. Panel 7 shows the magnetic pressure (red), ion thermal pressure (blue), and total pressure (black). The green box marks the sub-interval to be investigated hereafter.

electron pitch-angle distributions every 4–5 s and distribution function cuts based on its three-dimension distribution function measurements.

On 28 March 2016, at the duskside magnetopause, solar wind transport into the magnetosphere was observed by the two THEMIS spacecraft in a K-H vortex train when the IMF abruptly turned northward (Yan et al., 2020). The observational features of the K-H vortices such as the rotation of the plasma flow, high-speed low-density characteristics, as well as the distortion of the magnetopause were identified in the observations. Plasma transport across the magnetopause was observed using both the ion and electron fluxes. Figure 2 gives an overview of the vortex train observed by THEMIS-E. The first vortex in the vortex train was observed during the interval UT 22:23:00–22:25:00 by the downstream spacecraft THEMIS-E and the interval UT 22:23:10–22:24:10 was diagnosed as the transport region characterized by the coexistence of cold and hot plasmas. It was in this vortex that a substructure was found when the THEMIS-E was located at [1.9, 11.3, 2.4] Re (Earth's radius) in GSM coordinates, marked by the green box in Figure 2. As demonstrated below, further investigation of the vortex has revealed additional details of fine structures arising in the transport region.
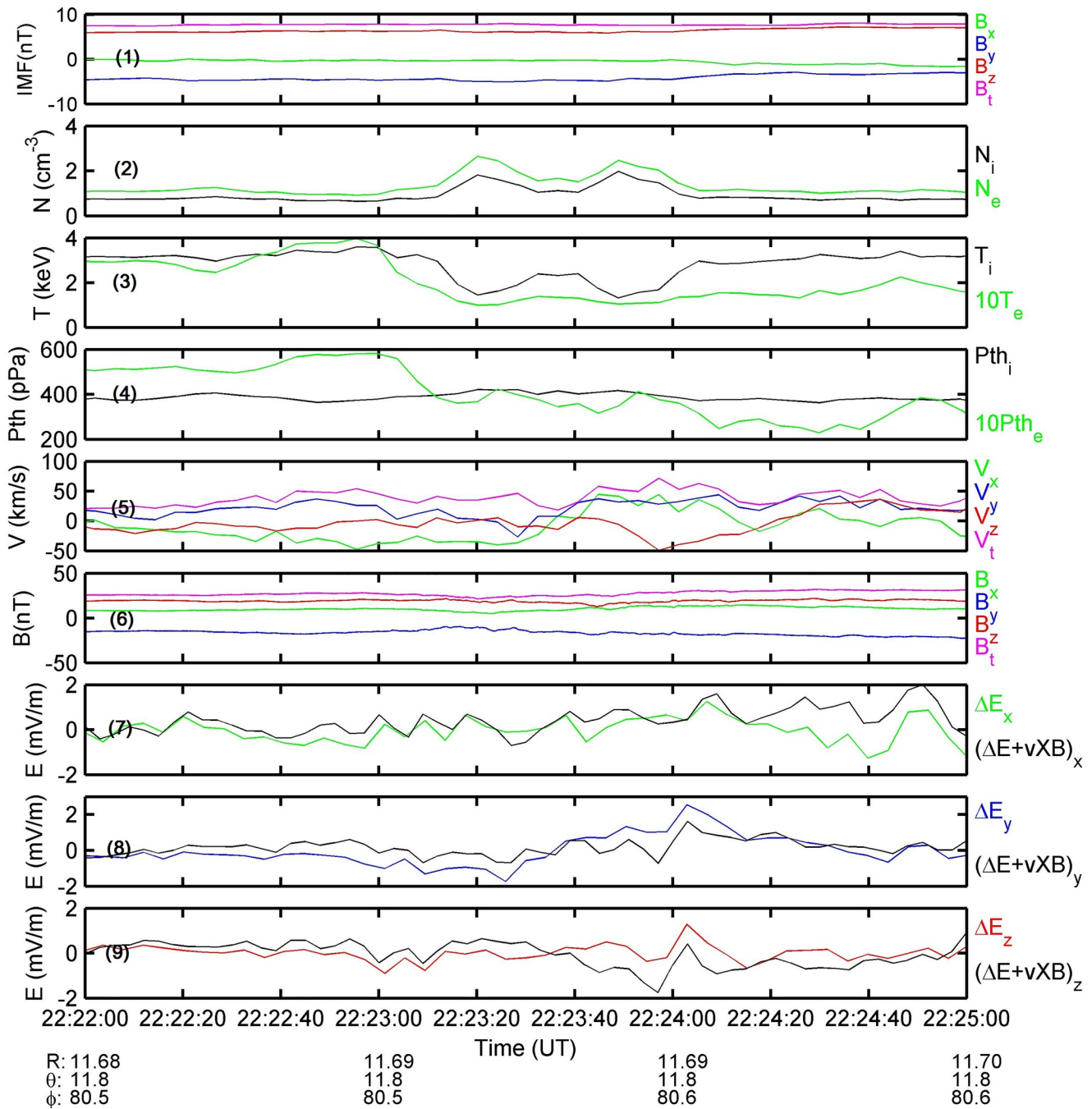
Figure 3. Measurements of the plasma and field parameters. In panel 1 shows the IMF conditions observed by THEMIS-B at lunar orbit, with a forward time shift of 10 min. All measurements from panel 2 to panel 9 are made by THEMIS E. Panel 2 presents the ion and electron densities. The temperatures of the ions (black) and electrons (green) are plotted in panel 3, and the ion (black) and electron (green) thermal pressures are plotted in panel 4. Panel 5 shows the three components and magnitude of the ion bulk velocity. Panel 6 shows the three components and magnitude of the magnetic field. Panel 7 shows the X component of the electric field (green) and the net electric field (black) after the convective electric field has been removed. Panel 8 shows the Y component of the electric field (blue) and the net electric field (black) after the convective electric field has been removed. Panel 9 shows the Z component of the electric field (red) and the net electric field (black) after removing the convective electric field. All vectors are in GSM coordinates.

Figure 3 shows the IMF conditions measured by THEMIS-B in lunar orbit and the plasma and field parameters measured by THEMIS-E. A time lag of 10 min is shifted forward from THEMIS-B at [−32.5, −46.8, −23.8] Re in GSM to the magnetopause. The IMF B_z is northward, and IMF B_y is dawnward, nearly as strong as B_z (panel 1). There are two increases in the ion and electron densities (panel 2), and correspondingly, there are two decreases

in the ion temperature (black line in panel 3). At the same time, the electron temperature (green line in panel 3) is nearly constant and low ($\sim$0.1 keV). The ion thermal pressure is quite steady (black line in panel 4), and there are also some small fluctuations in the electron thermal pressure (green line panel 4) within the vortex, with a slope of about 1 pPa s^{-1}. The magnitude of the bulk velocity is about 50 km s^{-1} (panel 5), much smaller than the estimated Alfvén speed V_A of about 450 km s^{-1}. The magnetic field in panel 6 appears to be very stable without noticeable fluctuations. The electric field ΔE_x (green), ΔE_y (blue), and ΔE_y (red), in panels 7, 8, and 9, are the three components of $\Delta E = E - E_{mean}$, respectively. The convective electric field $E_{conv} = -v \times B$, as well as the mean electric field E_{mean} during the interval have been removed to obtain the net electric field $E_1 = \Delta E + v \times B$, revealing perturbations of the electric field. The black lines in panels 7, 8, and 9 are the three components of the net electric field $\Delta E + v \times B$, respectively. In each panel, the difference between the colored lines and the black lines is the corresponding component of the convective electric field E_{conv}, which is very small because the velocity is only a few tens of km s^{-1} (panel 5). Because of the frame dependence of the electrostatic or inductive field (Borovsky, 2016), we remove the convective electric field to examine the electric field in the plasma frame of reference, and we remove the mean electric field to examine the perturbed electric field. The resulting wave-like variation in the net electric field E_1 is shown in panels 7, 8, and 9.

Figure 4 shows the ion pitch-angle distributions in 20 energy channels and the ion time-energy spectrogram (panel 21) during the vortex interval (panel 1–20). In panel 21, hot ions coexist with cold ions during the interval UT 22:23:10–22:24:10, which has been considered to be the time of the transport region in the vortices. The transport region splits into two parts, with two flux enhancements of cold plasma in a background of hot plasma. Such a feature is consistent with the two peaks in the ion density (panel 2 in Figure 3) and the two decreases in ion temperature (panel 3 in Figure 3), and clearly displays a substructure within the parent vortex. Before UT 22:23:10, the magnetospheric hot ions dominate in the energy channels above 1 keV (panels 1–12), representing the unperturbed magnetosphere. Within the vortex, the magnetospheric hot ions can be clearly seen in the three top channels 12.3–21.3 keV (panels 1–3), with pitch-angles mostly near 90°, showing that the hot ions are trapped on the magnetospheric field lines. In panels 4–12, the middle energy ions have lower fluxes in the channels 1–9 keV showing a transition to trapping. In panels 13–20, the cold ions from magnetosheath are conspicuous in the low energy channels. The cold ions are mainly distributed near 90°, implying that they are experiencing transverse motion. The cold ion distributions in the lower-energy channels 33.8–787.1 eV (panels 13–20) split into two parts within the vortex, consistent with the two enhancements of cold ion flux in the energy spectrogram (panels 21). The cold ion fluxes are observed for time duration of about 20 s. Using the fact that the tailward propagation of the K-H vortex is about 212 km s^{-1}, the size of the two fluxes can be estimated to be about 4,240 km, that is, 0.67 Re. Since the time duration of the cold ion fluxes is 20 s, and the spatial size of the substructure is about 4,240 km, the time resolution of 3 s is adequate to measure the structure. The proton gyro-period in the substructure is estimated to be about 1.3 s, much smaller than the instrumental resolution of 3 s and the resolution of pitch-angle distribution. Both the distribution function cuts (Figure 6) and the pitch-angle distribution are reliable. On the other hand, for different energy channels, the gyro-radius is estimated to be about 400 km for 21 keV, 90 km for 1 keV, and 15 km for the lowest channel at 33 eV. For the cold ions less than 1 keV, the gyro-radius is typically less than 90 km.

Figure 5 shows the electron time-energy spectrogram (panel 16) as well as the electron pitch-angle distributions in 15 energy channels within the vortex. There is no useful information in panels 1 and 2, because the data have insufficient resolution for this event. Similar to the ion distributions in Figure 4, during the transport region of UT 22:23:10–22:24:10, the hot and cold electrons coexist and there are two flux enhancements of the cold electron in time-energy spectrogram (panel 16), consistent with the two peaks in the electron density (panel 2 in Figure 3). The magnetospheric hot electrons dominate in energy channels above 500 eV (panels 3–7) before UT 22:23:10, which is in the unperturbed magnetosphere. Within the transport region, the magnetospheric hot electrons can be seen in panels 3–7, although the fluxes are lower in panels 4–7. The cold electrons are prominent in the channels under 500 eV (panels 8–15). However, electrons in different energy channels have different pitch-angle distributions. In the four channels 97–503 eV (panels 8–11), electrons are dominantly parallel and antiparallel to the magnetic field, that is, a counter streaming distribution. On the other hand, the cold electrons have significant fluxes near 90° with a bifurcated structure in the four lower-energy channels 10–55 eV (panels 12–15). The distributions of cold electrons perpendicular to the magnetic field imply that they might be also experiencing transverse motion. Despite the absence of data in the higher energy channels, the two flux enhancements of cold electron in the background of hot electrons (panel 16) are consistent with the two-enhancement structure in the
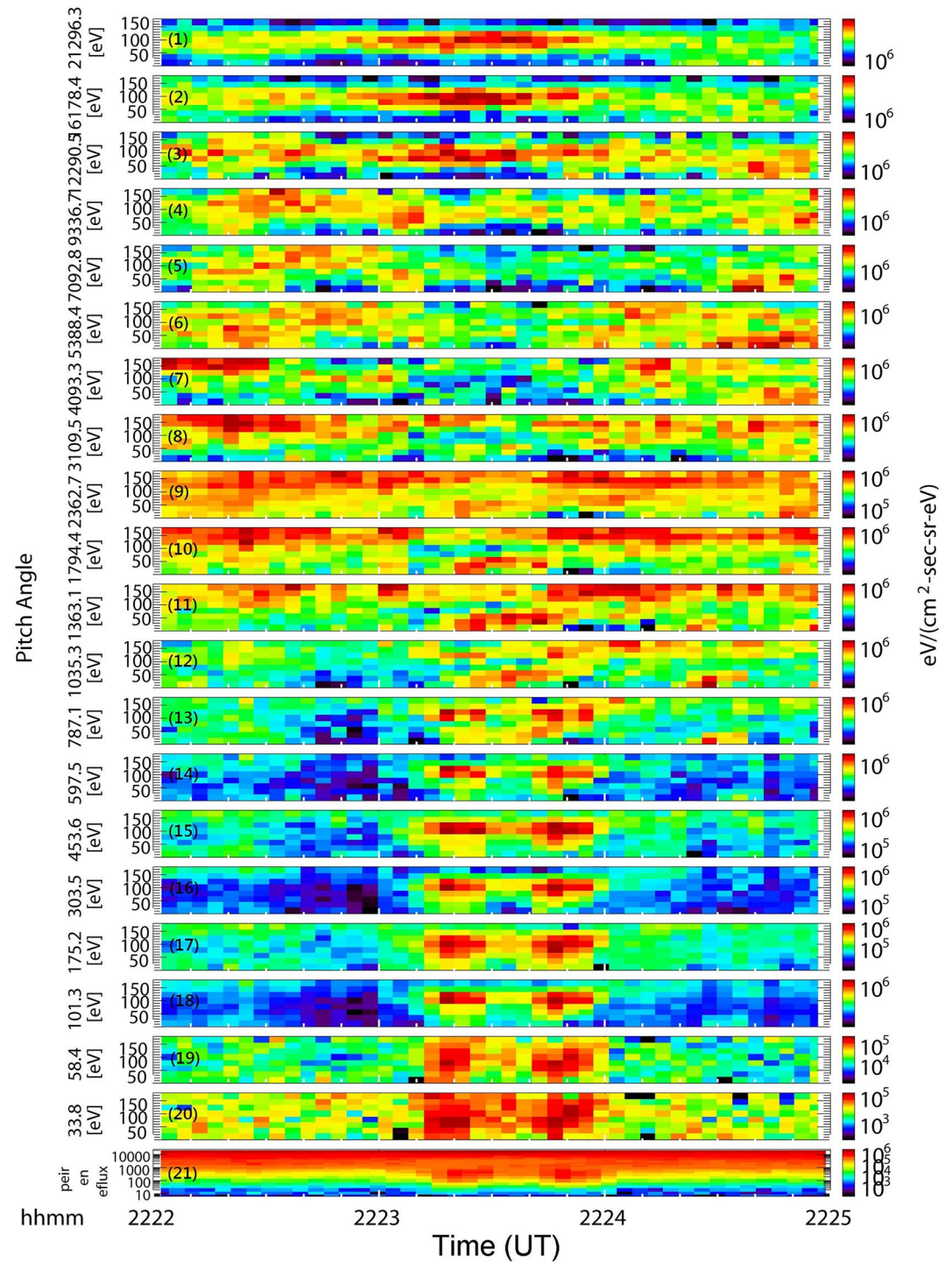
Figure 4. Ion pitch-angle distributions observed by TH-E. The top energy channel centered at 25.213 keV and the three lowest energy channels centered at 6.5, 11.3, and 19.4 eV are not shown because of an absence of data and contamination by photoelectrons. The center energy of each channel is marked on the left side of panels 1–20. The ion time-energy spectrum is presented in the bottom panel 21.
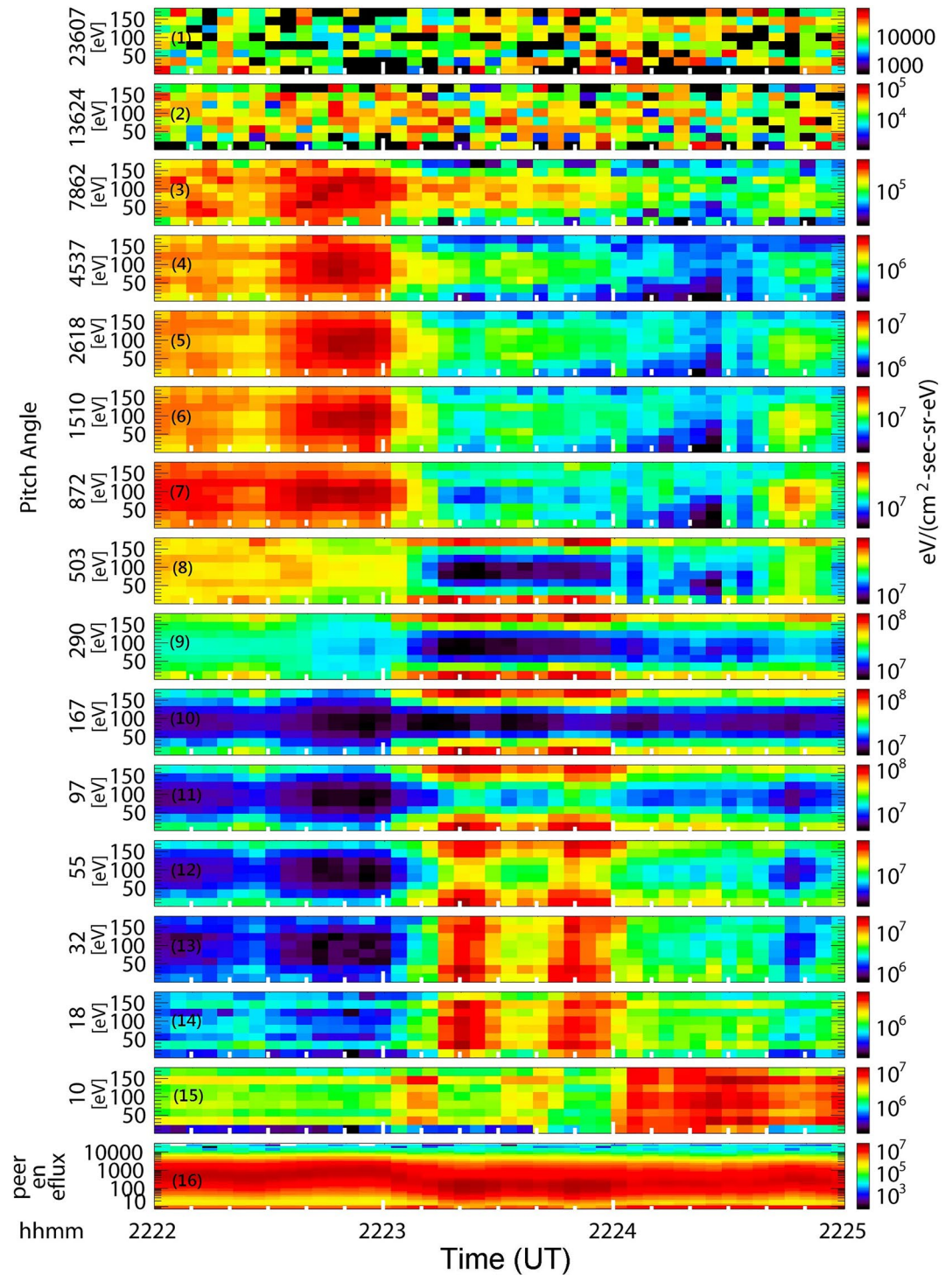
Figure 5. Electron pitch-angle distributions observed by TH-E. The center energy of each channel is marked on the left side of panels 1–15. Several high energy channels are removed due to an absence of data. The electron time-energy spectrum is presented in the bottom panel 16.
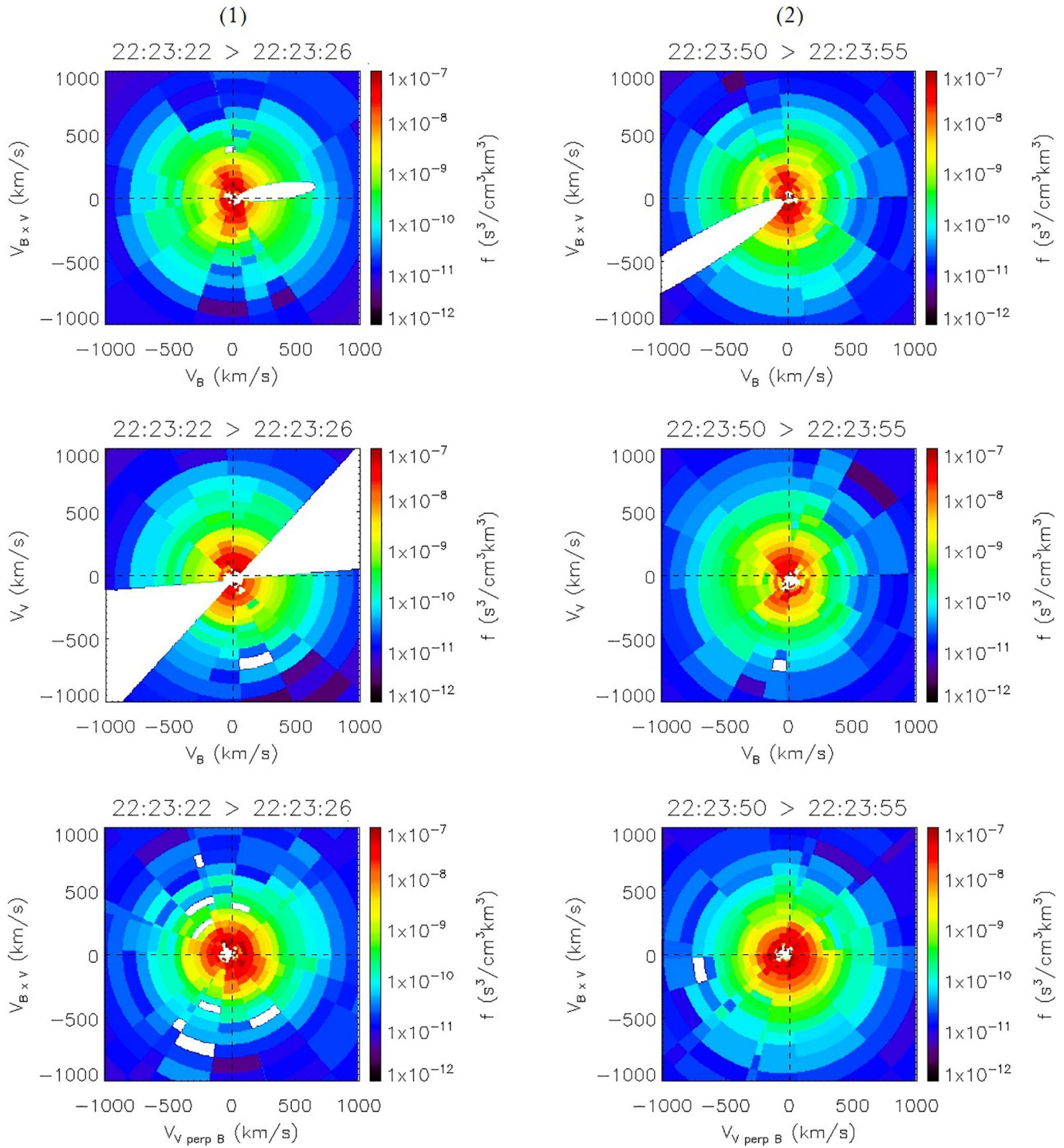
Figure 6. Ion distribution function cuts within the two flux enhancements based on the three-dimensional distribution function measurements of ESA onboard THEMIS-E, with the convective velocity subtracted. Panels 1 on the left and panel 2 on the right show the distribution function cuts in the planes of (V_B, $V_{B\times V}$) (upper), (V_B, $V_{(B\times V)\times B}$) (middle), and ($V_{(B\times V)\times B}$, $V_{B\times V}$) (lower) at UT 22:23:22–22:23:26 and UT 22:23:20–22:23:55, respectively.

pitch-angle distributions (panels 12–15). Both the cold ion and electron pitch-angle distributions show the splitting features in the transport region.

Figure 6 shows the ion distribution function cuts in the plane of $(V_B, V_{B \times V})$ (upper), $(V_B, V_{(B \times V) \times B})$ (middle), and $(V_{(B \times V) \times B}, V_{B \times V})$ (lower) within the two flux enhancements. Since the convective velocity has been subtracted, such distributions are depicted in the plasma frame of reference, revealing the kinetic behavior of the plasma in the vortex. In the ion distribution, three features can be seen: the substantial cold ions (yellow and red) superposed on the hot ions (cyan and green), indicating the coexistence of the two components; the elongated distribution along the perpendicular directions, indicating the temperature anisotropy (e.g., Hasegawa et al., 2003; Vernisse et al., 2016); the asymmetric dumbbell-shaped distributions in the plane of $(V_B, V_{B \times V})$ (upper), $(V_B, V_{(B \times V) \times B})$ (middle), indicating the transverse motion of the cold ions. The distributions in the dumbbells are asymmetrical along opposite directions, and the cold ions are distributed along the perpendicular direction with a net drift, implying that the motion of the cold ions doesn't counteract each other in the opposite directions perpendicular to $\boldsymbol{B}$. The distribution indicates that there is a transverse motion of the cold ions along a perpendicular direction, which is independent of the particle energy or temperature. Such a transverse motion is consistent with the pitch-angle distribution shown in Figure 4. On the other hand, circular distributions in the plane of $(V_{(B \times V) \times B}, V_{B \times V})$ (lower) show a gyrotropic feature of the cold ions in the perpendicular plane.

During the sub-interval of investigation, THEMIS-E is a downstream probe at the magnetopause near the terminator, THEMIS-A is an upstream probe at the magnetopause 3 Re away, and THEMIS-D is located much in the magnetosphere, even further away from the magnetopause. So it is inappropriate to analyze the spatial variation of the perturbed electric field.

3. Discussion

In this event, a local transport process must be responsible for the coexistence of the cold and hot plasmas displayed in Figures 3 and 4. The two flux enhancements of cold plasmas in the ion and electron spectrograms could be generated either by a secondary crossing of the rolled-up vortex or by the substructure within the parent vortex. Had the spacecraft secondarily crossed the rolled-up vortex in this event, the plasma parameters should coincidently change along with the shift of the background plasmas. During the traversal of the vortex, there are two increases in both ion and electron densities (panel 2 of Figure 3). However, the two decreases correspondingly appear in the ion temperature (black line in panel 3 of Figure 3) but not in the electron temperature (green line in panel 3 of Figure 3), thus excluding a secondary crossing of the rolled-up vortex along with reentry into the magnetosphere. Thus, the two flux enhancements of the cold plasma in the spectrograms can be interpreted as a substructure of the vortex. For the same reason, the coexistence of cold and hot plasmas ought to be caused by plasma transport rather than boundary layer oscillations, because there are corresponding decreases in the ion temperature while the electron temperature remains low within the substructure, indicating that there is no shift in the plasma background due to boundary oscillations. Therefore, it can be inferred that the two flux enhancements of cold plasmas in the spectrograms are more likely to be associated with convective cells driven by the charge separate electric field $\boldsymbol{E}_1$. The time scale of the substructure is about 40 s, approximately one third of the parent vortex's time scale of 2 min.

The substructure produced by the secondary K-H instability previously appeared in the MHD simulation along the boundary of the parent K-H vortex (Nakamura et al., 2004), with plasma mixing and the onset of turbulence. In the MHD simulation (Matsumoto & Hoshino, 2004), the secondary R-T instability was found to change the macroscopic structure of the boundary while the secondary K-H instability was merely a seed for turbulence. In their full particle simulation (Matsumoto & Hoshino, 2006), in addition to the reappearance of substructure along the K-H vortex boundary, the electrostatic potential indicated a charge separation electric field that was 4.0 times stronger than the convective electric field. The vital importance of the electrostatic field was stressed in the simulation. They obtained the absolute value as well as the time profile of the electrostatic field in their full particle simulation, and suggested that the strong electrostatic field scattered the ions and deformed the electron density interface in the secondary R-T instability. As mentioned above, the substructure of the K-H vortex has now been observed by THEMIS-E at the duskside magnetopause. In Figure 3, the perturbed electric field enhancement is larger than the convective electric field, similar to the earlier simulation results. Furthermore, the spatial profile of
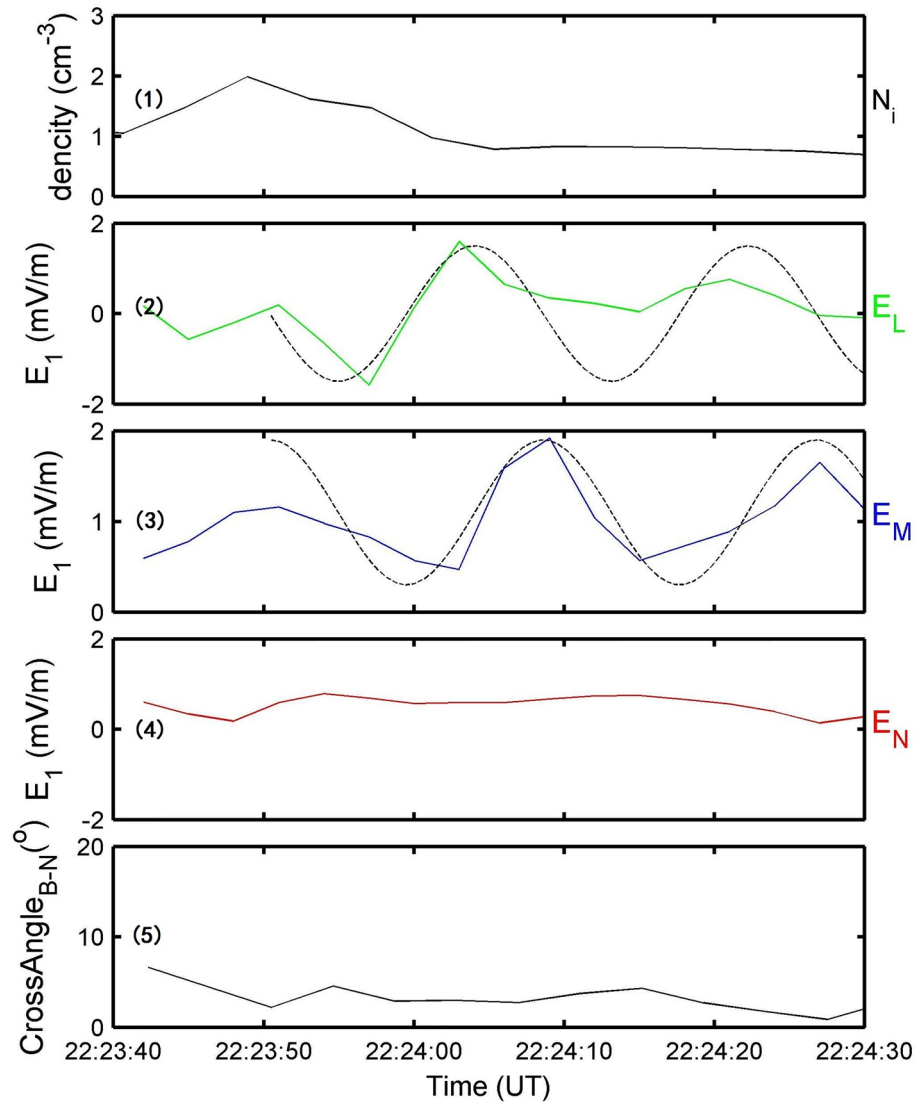
Figure 7. Sinusoidal spatial profiles of the net electric field $\mathbf{E_1}$ in the local coordinates LMN, in comparison with the ion density in panel 1. The three components of $\mathbf{E_1}$ are presented in panels 2–4, respectively. The cross angle between the magnetic field B and N direction are shown in panel 5. The dashed lines in panels 2 and 3 are the two sinusoidal signals having a phase difference of 90°, with the period of 18 s, the amplitude of 1.5 eV m^{-1} for E_L and 0.8 mV m^{-1} for E_M.

the electrostatic field has been observed, as shown in Figure 7 and discussed below. As the evidence of the plasma transport, the transverse motion of the cold plasmas has been observed in our event (Figures 4–6).

The two-enhancement features in the ion and electron pitch-angle distributions indicate the presence of substructure in the K-H vortex. The electron counter streaming is observed only at energies 97–503 eV (panels 8–11, in Figure 5) rather than at all energies, so we are not sure whether the field lines are open (Fuselier et al., 1997) or closed (Øieroset et al., 2008). However, the spacecraft should be located in the inner low-latitude boundary layer (LLBL). The distributions of cold ions and electrons near 90° imply transverse motion perpendicular to the magnetic field, and the asymmetric dumbbell-shaped ion distributions further indicate that the cold ions are undergoing a transverse motion. We remove the convective electric field to observe the electric field in the plasma frame of reference. If the plasmas were frozen with the magnetic field, there would not be any significant remaining electric field. However, with the convective electric field and the mean electric field removed, that is, observed in the plasma frame, a significant net electric field of several mV m^{-1} remains, implying a crucial role of the electric field in driving the transverse motion. The remnant electric field originates from either induction of changing magnetic field or charge separation.

For more insight into the electric field, we performed a minimum variance analysis (MVA; Sonnerup & Cahill, 1967, 1968; Sonnerup et al., 1987) on the net electric field E_1 to calculate the local orthogonal coordinates LMN, in which the net electric field E_1 is expressed. The MVA results show a ratio $r_{23} = \varepsilon_2/\varepsilon_3$ of 6.3, the L direction of (0.1589, 0.7680, 0.6204), M direction of (0.9333, 0.0882, −0.3482) and N direction of (0.3221, −0.6343, 0.7027), closely consistent with the illustration in panel 2 of Figure 1. The panel 1 gives the ion density, and panels 2–4 of Figure 7 show the net electric field E_1 in the LMN coordinates, E_L, E_M, E_N, and panel 4 presents the cross angle between N and the magnetic field B, respectively. The dashed lines in panels 1 and 2 are the sinusoidal signals with a phase difference of 90°. The observed E_N is very small, which is aligned to the magnetic field B with the cross angle less than 5° (panel 4). The E_L and E_M fit the sinusoidal signals quite well (panels 1, 2), indicating typical variations in the perpendicular plane. In other words, we found a local coordinate system LMN to display the net electric field, in which the N direction is closely aligned to the magnetic field and the variations of the net electric field in L and M show typical sinusoidal forms with a 90° phase difference. The period of the sinusoidal signals is 18 s, and the amplitude is 1.5 mV m^{-1} for E_L and 0.8 mV m^{-1} for E_M, totally about 1.7 mV m^{-1}. According to Equation 2, with $\frac{4\pi\sigma}{\varepsilon} \approx 1$ mV/m, the surface charge density on the boundary can be estimated as 4.4×10^{-1} cm^{-2}, and the volume density is correspondingly 4.4×10^{-1} cm^{-3}, which is much smaller than the observed ion and electron density by one order, indicating that only a small fraction of ions separate from electrons. The tailward propagation speed of the vortex train can be estimated as 212 km s^{-1} by calculating the separation of 3 Re (earth radius) between the spacecraft THEMIS-A and THEMIS-E and the time lag of 90 s from THEMIS-A to THEMIS-E (Yan et al., 2020). With the tailward propagation speed, we can in turn estimate the wavelength of the electric field perturbation to be about 3,800 km, that, 0.60 Re. Since the period of the sinusoidal signals is 18 s, the electric field perturbation calculated from the 3-s time resolution EFI data is adequate to measure the substructure and its signal.

The variations of the net electric field E_1 at the trailing edge of the substructure satisfy a Poisson equation with the charge distribution shown in panel 1 of Figure 1, in accordance with the classical model of the R-T instability (Parks, 2003). The magnetic field is steady without fluctuations; hence, the charge separation during an instability such as the R-T instability is the most likely candidate for generating the electric field perturbation. The detection of a perturbed electric field E_1, as shown in Figure 7, matches the theoretical prediction of the R-T instability in Equation 2 very well and will thus produce the substructure of the K-H vortex. Consequently, we suppose that the perturbed sinusoidal electric field is an additional electric field that arises from the transient charge separation at the boundary when the R-T instability grows. For the configuration within the K-H vortex, it is stable where the magnetopause boundary is convex to the magnetosheath, while unstable where the magnetopause boundary is convex to the magnetosphere. Sufficient centrifugal force and density gradient are necessary to drive a complex frequency. The substructure in Figure 1 (panel 2) is located at the most favorable part of the vortex.

In this event, although a secondary K-H vortex could also be excited at the edge of the parent K-H vortex, we did not find an adequate thermal pressure gradient that could act as the counterpart of the perturbed electric field E_1 and drive such a secondary K-H vortex. Furthermore, the electron thermal pressure is pretty steady within the vortex, only changing at a rate of about 1 pPa s^{-1} (green line in panel 4 of Figure 3). Since a single spacecraft cannot discern the spatial variation from the temporal variation, it is difficult to accurately calculate the electron thermal pressure gradient and compute the gradient electric field. But the electron thermal pressure gradient can be roughly estimated by omitting the temporal variation, that is, $\frac{dp_e}{dt} = \frac{\partial p_e}{\partial t} + v \cdot \frac{\partial p_e}{\partial r} \approx v \cdot \frac{\partial p_e}{\partial r}$. Thus, with $n_e = 2.7$ cm^{-3}, $v = 50$ km s^{-1}, the gradient electric field $\frac{-\nabla p_e}{n_e e}$ can be estimated to be about 4.6×10^{-2} mV m^{-1}, much two orders of magnitude lower than the observed electric field perturbation. The negligible gradient electric field implies that the smaller-scale terms such as the electron inertia item in the generalized Ohm's law is too small to produce the secondary K-H vortices (Nakamura et al., 2004). The lower-hybrid drift instability (LHDI) is another candidate that may generate substructure and drive the plasma transport across the magnetic field lines. However, the frequency of LHDI should be much lower than the electron gyro frequency of a few kHz but much higher than the ion gyro frequency of a few Hz (Gary & Eastman, 1979). The observed electric field perturbation of 18 s does not match the theoretical frequency of the LHDI. As for the low-frequency drift instability (LFDI) below the ion gyro frequency (Patel, 1978), which may also form the substructure of convective cells, the density perturbation should have the same phase as the electric field perturbation that drives the plasma transport (e.g., Cai et al., 2009). But the THEMIS-E observations in Figure 7 show a clear phase difference between the density perturbation and the electric field perturbation. At the same time, with the background of rotation flows and the

centrifugal force, we suggest that a secondary R-T instability is the most likely candidate, as illustrated in panel 2 of Figure 1.

As soon as the IMF abruptly turns from duskward to northward, the K-H waves are excited and the first vortex arrives at THEMIS-E, with the concomitant plasma rotation. The centrifugal force of such rotation causes the non-electromagnetic force drift, in which the electrons and ions drift in opposite directions and hence separate from each other along the boundary. The charge separation gives rise to electric field E_1, and then the electrostatic field drives the transverse motion of the plasma by electric drift $E_1 \times B$. When R-T instability is activated, driven by the centrifugal force drift, only a small fraction of charges need to separate from each other to generate sufficient electrostatic field, as indicated by the estimated surface charge density. Such electrostatic field can work only on the nearby plasmas rather than on the separated charges themselves by driving the $E_1 \times B$ drift. It is via such a collective behavior of plasmas that the small fraction of the plasma responds to the rotating motion in the vortex to generate the electrostatic field to drive the $E_1 \times B$ drift of other ambient plasmas across the magnetic field. The substructure moves tailward along with the tailward propagation of the K-H vortex, and the spatial profile of the perturbed electric field is recorded by the spacecraft when the substructure is encountered. The sinusoidal perturbed electric field E_1 is the accompanying feature of the secondary process and ultimately drives plasma transport across the magnetopause.

On the other hand, the magnetic field varies little within the vortex, implying that the magnetic configuration doesn't change. The absence of plasma jets in the observations comparable to the Alfvénic velocity V_A excludes magnetic reconnection during this event. At the magnetopause, the K-H waves can couple to KAWs and cause anomalous transport across the magnetic field (Chaston et al., 2007). Some theoretical analyses have shown that the KAWs involve both perpendicular and parallel electric field components (Hollweg, 1999), however, it is the parallel electric field of a few $\mu V\,m^{-1}$ carried by the KAWs that causes plasma transport. The typical wavelength of the KAWs at the magnetopause is about 100 km, comparable to the ion gyro radius (Chaston et al., 2007; Johnson & Cheng, 2001). But the observed wavelength of the electrostatic field is 3,800 km. The KAWs could cause perpendicular heating of low energy ions (Johnson & Cheng, 2001; Wing et al., 2005), which is one of the characteristics of KAWs. In the present event, the perpendicular ion temperature is higher than the parallel temperature as shown in the distribution function (Figure 6), but the heating of the cold ions is difficult to verify by comparing to the distribution simultaneously in the magnetosheath, because the spacecraft THEMIS-E is located in the inner LLBL. Therefore, although the KAW mechanism within K-H vortices cannot be completely precluded, such a mechanism could not explain the observations such as the wavelength of nearly 4,000 km and the steady magnetic field without significant fluctuations in this event. Similarly, the period of 18 s in E_1 cannot match the typical characteristics of kinetic magnetosonic waves with wavelength of about 200 km, as reported previously by Moore et al., 2016.

We have identified plasma transport within the K-H vortex and found that substructure is present both from the spectrograms and the pitch-angle distributions. The accompanying electric field E_1 appears to confirm the predicted observational features of a secondary R-T instability with substructure as illustrated in panel 2 of Figure 1. The frozen-in condition has been violated once the charges are separated during the centrifugal force drift. Thus the charge separate electric field E_1 drives the plasma to move across the magnetic field lines by $E_1 \times B$ drift and consequently forms the convective cells of the substructure as observed in the pitch-angle distributions by THEMIS-E. Therefore, the $E_1 \times B$ drift could explain the transverse motion of the cold plasmas, and such observations show a convective perturbation pattern. On the other hand, the magnetospheric plasma could also emerge out of the magnetopause and form a halo (Sckopke et al., 1981) or a streaming layer (Sibeck, 1992). Consequently, the secondary R-T instability appears to provide a way for plasma exchange to occur across the magnetopause within the K-H vortex.

4. Conclusions

Based on detailed investigations of the first vortex in a train of K-H vortices at the duskside magnetopause under northward IMF, we have identified a substructure of the K-H vortex that shows a bifurcated feature two enhancements in the ion and electron pitch-angle distributions, consistent with the two increases in ion density and the two decreases in ion temperature. The transverse motion of cold plasmas has been observed in the pitch-angle distributions, implying ongoing plasma transport into the magnetosphere. The accompanying electric field of the

secondary R-T instability within the parent K-H vortex has been detected and the spatial profile of the electric field in sinusoidal forms has been recorded, which satisfies the theoretical prediction quite well. The perturbed electric field is expected to be an electrostatic field due to the charge separation when the R-T instability produces the substructure seen in the K-H vortex. The transverse motion of cold plasmas indicates that the perturbed electric field drives the plasma motion by the $E_1 \times B$ drift. The observations strongly support the previous simulation results that a secondary R-T instability within the parent K-H vortex causes the plasma transport across the magnetopause. This result is the first observational evidence for such a transport mechanism and the verification of the earlier simulation results of Matsumoto and Hoshino (2004, 2006), Nykyri and Otto (2004), and Cowee et al. (2009). The necessary conditions, such as the velocity shear, the centrifugal force, and the sharp density gradient to activate the instabilities are confined to the thin boundary layer. Hence, the plasma transport driven by the R-T instability within K-H vortices could be localized close to that thin boundary. The plasma motion across the magnetic field will stop where the electrostatic field disappears. The entering cold plasma, pushed across the magnetopause by the electrostatic field, will participate in the convection along with the magnetic field in the inner magnetosphere. Since only THEMIS-E encounters the substructure, the electrostatic field E_1 is "single-tracked." It would be of great significance to further investigate such a secondary process when at least two spacecraft are within typical ion inertial radius, in which case the "stereo" recording of the electrostatic field could reveal more details, including the possible plasma instabilities.

Data Availability Statement

The data for this paper are available at the THEMIS data website (https://themis.ssl.berkeley.edu/data/themis/) and the Coordinated Data Analysis Web of NASA's Goddard Flight Center (https://cdaweb.gsfc.nasa.gov/istp_public/).

References

Adamson, E., Nykyri, K., & Otto, A. (2016). The Kevin-Helmholtz instability under Parker-Spiral interplanetary magnetic field conditions at the magnetospheric flanks. *Advances in Space Research*, *58*, 218–230. https://doi.org/10.1016/j.asr.2015.09.013

Angelopoulos, V. (2008). The THEMIS mission. *Space Science Reviews*, *141*, 5–34. https://doi.org/10.1007/s11214-008-9336-1

Auster, U., Glassmeier, K. H., Magnes, W., Aydogar, O., Baumjohann, W., Constaninescu, D., et al. (2008). The THEMIS fluxgate magnetometer. *Space Science Reviews*, *141*, 235–264. https://doi.org/10.1007/s11214-008-9365-9

Bonnell, J. W., Mozer, F. S., Delory, G. T., Hull, A. J., Ergun, R. E., Cully, C. M., et al. (2008). The electric field instrument (EFI) for THEMIS. *Space Science Reviews*, *141*, 303–341. https://doi.org/10.1007/s11214-008-9469-2

Borovsky, J. E. (2016). Relativity and the solar wind: The Maxwell-Equation origins of the solar-wind motional electric field. *Journal of Electromagnetic Analysis and Applications*, *8*, 133–151. https://doi.org/10.4236/jemaa.2016.88014. http://dx.doi.org/10.4236/jemaa.88014

Cai, C. L., Dandouras, I., Rème, H., Cao, J. B., Zhou, G. C., Shen, C., et al. (2009). Magnetosheath excursion and the relevant transport process at the magnetopause. *Annals in Geophysics*, *27*, 2997–3005. https://doi.org/10.5194/angeo-27-2997-2009

Chandrasekhar, S. (1961). *Hydrodynamic and hydromagnetic stability*. Clarendon Press.

Chaston, C. C., Wilber, M., Mozer, F. S., Fujimoto, M., Goldstein, M. L., Acuna, M., et al. (2007). Mode conversion and anomalous transport in Kelvin-Helmholtz vortices and kinetic Alfvén waves at the Earth's magnetopause. *Physical Review Letters*, *99*, 175004. https://doi.org/10.1103/PhysRevLett.99.175004

Chen, S.-H., & Kivelson, M. G. (1993). On nonsinusoidal waves at the magnetopause. *Geophysical Research Letters*, *20*, 2699–2702. https://doi.org/10.1029/93gl02622

Chen, S.-H., Kivelson, M. G., Gosling, J. T., Walker, R. J., & Lazarus, A. J. (1993). Anomalous aspects of magnetosheath flow and of the shape and oscillations of the magnetopause during an interval of strongly northward interplanetary magnetic field. *Journal of Geophysics*, *98*, 5727–5742. https://doi.org/10.1029/92ja02263

Cowee, M. M., Winske, D., & Gary, S. P. (2009). Two-dimensional hybrid simulations of superdiffusion at the magnetopause driven by Kelvin-Helmholtz instability. *Journal of Geophysical Research*, *114*, A10209. https://doi.org/10.1029/2009JA014222

Dai, L. (2009). Collisionless magnetic reconnection via Alfvén Eigenmodes. *Physical Review Letters*, *102*, 245003. https://doi.org/10.1103/PhysRevLett.102.245003

Dai, L. (2018). Structures of Hall fields in asymmetric magnetic reconnections. *Journal of Geophysical Research: Space Physics*, *123*(9), 7332–7341. https://doi.org/10.1029/2018JA025251

Dai, L., Wang, C., Zhang, Y., Lavraud, B., Burch, J., Pollock, C., & Torbert, R. B. (2017). Kinetic Alfvén wave explanation of the Hall fields in magnetic reconnection. *Geophysical Research Letters*, *44*, 634–640. https://doi.org/10.1002/2016GL071044

Dungey, J. W. (1961). Interplanetary magnetic field and auroral zones. *Physical Review Letters*, *6*(2), 47–48. https://doi.org/10.1103/physrevlett.6.47

Eriksson, S., Lavraud, B., Wilder, F. D., Stawarz, J. E., Giles, B. L., Burch, J. L., et al. (2016). Magnetospheric multiscale observations of magnetic reconnection associated with Kelvin-Helmholtz waves. *Geophysical Research Letters*, *43*, 5606–5615. https://doi.org/10.1002/2016GL068783

Faganello, M., & Califano, F. (2017). Magnetized Kelvin-Helmholtz instability: Theory and simulations in Earth's magnetosphere context. *Journal of Plasma Physics*, *83*, 535830601. https://doi.org/10.1017/S0022377817000770

Farrugia, C. J., Gratton, F. T., Gnavi, G., Torbert, R. B., & Wilson, L. B. (2014). A vortical dawn flank boundary layer for near-radial IMF: Wind observations on 24 October 2001. *Journal of Geophysical Research: Space Physics*, *119*, 4572–4590. https://doi.org/10.1002/2013JA019578

Fujimoto, M., Tonooka, T., & Mukai, T. (2003). Vortex-like fluctuations in the magnetotail flanks and their possible roles in plasma transport. In P. T. Newell & T. Onsager (Eds.), *Earth's low-latitude boundary layer. Geophysical Monograph Series* (Vol. 133, pp. 241–251). AGU. https://doi.org/10.1029/133gm24

Fuselier, S. A., Anderson, B. J., & Onsager, T. G. (1997). Electron and ion signatures of field line topology at the low-shear magnetopause. *Journal of Geophysical Research*, *102*, 4847–4863. https://doi.org/10.1029/96ja03635

Gary, S. P., & Eastman, T. E. (1979). The lower hybrid drift instability at the magnetopause. *Journal of Geophysical Research: Space Physics*, *84*(A12), 7378–7381. https://doi.org/10.1029/ja084ia12p07378

Grygorov, K., Němeček, Z., Šafránková, J., Přech, L., Pi, G., & Shue, J.-H. (2016). Kelvin-Helmholtz wave at the subsolar magnetopause boundary layer under radial IMF. *Journal of Geophysical Research: Space Physics*, *121*, 9863–9879. https://doi.org/10.1002/2016JA023068

Guo, X. C., Wang, C., & Hu, Y. Q. (2010). Global MHD simulation of the Kelvin-Helmholtz instability at the magnetopause for northward interplanetary magnetic field. *Journal of Geophysical Research*, *115*, A10218–n. https://doi.org/10.1029/2009JA015193

Hasegawa, H., Fujimoto, M., Maezawa, K., Saito, Y., & Mukai, T. (2003). Geotail observations of the dayside outer boundary region: IMF control and dawn-dusk asymmetry. *Journal of Geophysical Research*, *108*(A4), 1163. https://doi.org/10.1029/2002JA009667

Hasegawa, H., Fujimoto, M., Phan, T.-D., Rème, H., Balogh, A., Dunlop, M. W., et al. (2004). Transport of solar wind into Earth's magnetosphere through rolled-up Kelvin-Helmholtz vortices. *Nature*, *430*, 755–758. https://doi.org/10.1038/nature02799

Hashimoto, C., & Fujimoto, M. (2005). Kelvin-Helmholtz instability in an unstable layer of finite thickness. *Advances in Space Research*, *37*, 527–531.

Hollweg, J. V. (1999). Kinetic Alfvén wave revisited. *Journal of Geophysical Research*, *104*(A7), 14811–14819. https://doi.org/10.1029/1998JA900132

Hwang, K.-J., Goldstein, M. L., Kuznetsova, M. M., Wang, Y., Viñas, A. F., & Sibeck, D. G. (2012). The first in situ observation of Kelvin-Helmholtz waves at high-latitude magnetopause during strongly dawnward interplanetary magnetic field conditions. *Journal of Geophysical Research*, *117*, A08233. https://doi.org/10.1029/2011JA017256

Hwang, K.-J., Kuznetsova, M. M., Sahraoui, F., Goldstein, M. L., Lee, E., & Parks, G. K. (2011). Kelvin-Helmholtz waves under southward interplanetary magnetic field. *Journal of Geophysical Research*, *116*, A08210. https://doi.org/10.1029/2011JA016596

Johnson, J. R., & Cheng, C. Z. (1997). Kinetic Alfvén waves and plasma transport at the magnetopause. *Geophysical Research Letters*, *24*, 1423–1426. https://doi.org/10.1029/97GL01333

Johnson, J. R., & Cheng, C. Z. (2001). Stochastic ion heating at the magnetopause due to kinetic Alfvén waves. *Geophysical Research Letters*, *28*(23), 4421–4424. https://doi.org/10.1029/2001GL013509

Johnson, J. R., Wing, S., & Delamere, P. A. (2014). Kelvin Helmholtz instability in planetary magnetospheres. *Space Science Reviews*, *184*, 1–31. https://doi.org/10.1007/s11214-014-0085-z

Kavosi, S., & Raeder, J. (2015). Ubiquity of Kelvin-Helmholtz waves at Earth's magnetopause. *Nature Communications*, *6*, 7019. https://doi.org/10.1038/ncomms8019

Kivelson, M. G., & Chen, S. H. (1995). The magnetopause: Surface waves and instabilities and their possible dynamic consequences. In P. Song, B. O. Ü. Sonnerup, M. F. Thomsen, & p. (Eds.), *Physics of the magnetopause* (Vol. 90, p. 257). AGU.*Geophysical Monograph Series*.

Li, W. Y., Guo, X. C., & Wang, C. (2012). Spatial distribution of Kelvin-Helmholtz instability at low-latitude boundary layer under different solar wind speed conditions. *Journal of Geophysical Research*, *117*, A08230–n. https://doi.org/10.1029/2012JA017780

Lu, S. W., Wang, C., Li, W. Y., Tang, B. B., Torbert, R. B., Giles, B. L., et al. (2019). Prolonged Kelvin-Helmholtz waves at dawn and dusk flank magnetopause: Simultaneous observations by MMS and THEMIS. *The Astrophysical Journal*, *875*, 57. https://doi.org/10.3847/1538-4357/ab0e76

Ma, X., Delamere, P., Otto, A., & Burkholder, B. (2017). Plasma transport driven by the three-dimensional Kelvin-Helmholtz instability. *Journal of Geophysical Research Atmospheres*, *122*, 10382–10410. https://doi.org/10.1002/2017JA024394

Ma, X., Delamere, P., Otto, A., Nykyri, K., Burkholder, B., Neupane, R. C., et al. (2019). Comparison between fluid simulation with test particles and hybrid simulation for the Kelvin-Helmholtz instability. *Journal of Geophysical Research: Space Physics*, *124*, 6654–6668. https://doi.org/10.1029/2019ja026890

Ma, X., Otto, A., Delamere, P. A., & Zhang, H. (2016). Interaction between reconnection and Kelvin-Helmholtz at the high-latitude magnetopause. *Advances in Space Research*, *58*, 231–239. https://doi.org/10.1016/j.asr.2016.02.025

Masson, A., & Nykyri, K. (2018). Kelvin-Helmholtz instability. *Lessons Learned and Ways Forward*, *214*, 71–89. https://doi.org/10.1007/s11214-018-0505-6

Matsumoto, Y., & Hoshino, M. (2004). Onset of turbulence induced by a Kelvin-Helmholtz vortex. *Geophysical Research Letters*, *31*, L02807. https://doi.org/10.1029/2003GL018195

Matsumoto, Y., & Hoshino, M. (2006). Turbulent mixing and transport of collisionless plasmas across a stratified velocity shear layer. *Journal of Geophysical Research*, *111*, A05213. https://doi.org/10.1029/2004JA010988

McFadden, J. P., Carlson, C. W., Larson, D., Ludlam, M., Abiad, R., Elliott, B., et al. (2008). The THEMIS ESA plasma instrument and in-flight calibration. *Space Science Reviews*, *141*, 277–302. https://doi.org/10.1007/s11214-008-9440-2

Miura, A. (1987). Simulation of Kelvin-Helmholtz instability at the magnetospheric boundary. *Journal of Geophysical Research*, *92*(A4), 3195–3206. https://doi.org/10.1029/ja092ia04p03195

Miura, A. (1992). Kelvin-Helmholtz instability at the magnetospheric boundary: Dependence on the magnetosheath sonic Mach number. *Journal of Geophysical Research*, *97*(A7), 10655–10675. https://doi.org/10.1029/92ja00791

Miura, A. (1995). Dependence of the magnetopause Kelvin-Helmholtz instability on the orientation of the magnetosheath magnetic field. *Geophysical Research Letters*, *22*(21), 2993–2996. https://doi.org/10.1029/95gl02793

Miura, A. (1999a). Self-organization in the two-dimensional magnetohydrodynamic transverse Kelvin-Helmholtz instability. *Journal of Geophysical Research*, *104*(A1), 395–411. https://doi.org/10.1029/98ja02530

Miura, A. (1999b). A quantitative test of the self-organization hypothesis of the magnetopause Kelvin-Helmholtz instability as an inverse problem. *Geophysical Research Letters*, *26*(3), 409–412. https://doi.org/10.1029/1998gl900300

Moore, T. W., Nykyri, K., & Dimock, A. P. (2016). Cross-scale energy transport in space plasmas. *Nature Physics*, *12*, 1164–1169. https://doi.org/10.1038/NPHYS3869

Nakamura, T. K. M., Eriksson, S., Hasegawa, H., Zenitani, S., Li, W. Y., Genestreti, K. J., et al. (2017). Mass and energy transfer across the Earth's magnetopause caused by vortex-induced reconnection. *Journal of Geophysical Research: Space Physics*, *122*, 11505–11522. https://doi.org/10.1002/2017JA024346

Nakamura, T. K. M., Hasegawa, H., Daughton, W., Eriksson, S., Li, W. Y., & Nakamura, R. (2017). Turbulent mass transfer caused by vortex induced reconnection in collisionless magnetospheric plasmas. *Nature Communications*, *8*, 1582. https://doi.org/10.1038/s41467-017-01579-0

Nakamura, T. K. M., Hayashi, D., & Fujimoto, M. (2004). Decay of MHD-scale Kevin-Helmholtz vortices mediated by parasitic electron dynamics. *Physical Review Letters*, *92*(14), 145001. https://doi.org/10.1103/physrevlett.92.145001

Nykyri, K., & Otto, A. (2001). Plasma transport at the magnetospheric boundary due to reconnection in Kelvin-Helmholtz vortices. *Geophysical Research Letters*, *28*, 3565–3568. https://doi.org/10.1029/2001gl013239

Nykyri, K., & Otto, A. (2004). Influence of the Hall term on KH instability and reconnection inside KH vortices. *Annals in Geophysics*, *22*, 935–949. https://doi.org/10.5194/angeo-22-935-2004

Nykyri, K., Otto, A., Lavraud, B., Mouikis, C., Kistler, L. M., Balogh, A., & Rème, H. (2006). Cluster observations of reconnection due to the Kelvin-Helmholtz instability at the dawnside magnetosphere flank. *Annals in Geophysics*, *24*, 2619–2643. https://doi.org/10.5194/angeo-24-2619-2006

Øieroset, M., Phan, T. D., Angelopoulos, V., Eastwood, J. P., McFadden, J., Larson, D., et al. (2008). THEMIS multi-spacecraft observations of magnetosheath plasma penetration deep into the dayside low-latitude magnetosphere for northward and strong by IMF. *Geophysical Research Letters*, *35*, L17S11. https://doi.org/10.1029/2008GL033661

Otto, A., & Fairfield, D. H. (2000). Kelvin-Helmholtz instability at the magnetotail boundary: MHD simulation and comparison with geotail observations. *Journal of Geophysical Research*, *105*(A9), 21175–21190. https://doi.org/10.1029/1999ja000312

Parks, G. K. (2003). *Physics of space plasma: An introduction*. Westview Press.

Patel, V. L. (1978). Low frequency drift oscillations near the plasmapause. *Geophysical Research Letters*, *5*(4), 291–293. https://doi.org/10.1029/gl005i004p00291

Rosenbluth, M. N., & Longmire, C. L. (1957). Stability of plasmas confined by magnetic fields. *Annals of Physics*, *1*(2), 120–140. https://doi.org/10.1016/0003-4916(57)90055-6

Sckopke, N., Paschmann, G., Haerendel, G., Sonnerup, B. U. Ö., Bame, S. J., Forbes, T. G., et al. (1981). Structure of the low-latitude boundary layer. *Journal of Geophysical Research*, *86*(A4), 2099–2110. https://doi.org/10.1029/ja086ia04p02099

Sibeck, D. G. (1992). Transient event in the outer magnetosphere: Boundary waves or flux transfer event? *Journal of Geophysical Research*, *97*(A4), 4009–4026. https://doi.org/10.1029/91ja03017

Song, P., & Russell, C. T. (1992). Model of the formation of the low-latitude-boundary-layer for strongly northward interplanetary magnetic field. *Journal of Geophysical Research*, *97*(A2), 1411–1420. https://doi.org/10.1029/91JA02377

Sonnerup, B. U. Ö., & Cahill, L. J. (1967). Magnetopause structure and attitude from Explorer 12 observations. *Journal of Geophysical Research*, *72*, 171–183. https://doi.org/10.1029/jz072i001p00171

Sonnerup, B. U. Ö., & Cahill, L. J. (1968). Explorer 12 observations of the magnetopause current layer. *Journal of Geophysical Research*, *73*, 1757–1770. https://doi.org/10.1029/ja073i005p01757

Sonnerup, B. U. Ö., Papamastorakis, I., Paschmann, G., & Lühr, H. (1987). Magnetopause properties from AMPTE/IRM observations of the convection electric field: Method development. *Journal of Geophysical Research*, *92*, 12137–12159. https://doi.org/10.1029/ja092ia11p12137

Takagi, K., Hashimoto, C., Hasegawa, H., Fujimoto, M., & TanDokoro, R. (2006). Kelvin-Helmholtz instability in a magnetotail flank-like geometry: Three-dimensional MHD simulations. *Journal of Geophysical Research*, *111*, A08202. https://doi.org/10.1029/2006JA011631

Vernisse, Y., Lavraud, B., Eriksson, S., Gershman, D. J., Dorelli, J., Pollock, C., et al. (2016). Signatures of complex magnetic topologies from multiple reconnection sites induced by Kelvin-Helmholtz instability. *Journal of Geophysical Research: Space Physics*, *121*, 9926–9939. https://doi.org/10.1002/2016JA023051

Walsh, B. M., Thomas, E. G., Hwang, K.-H., Baker, J. B. H., Ruohoniemi, J. M., & Bonnell, J. W. (2015). Dense plasma and Kelvin-Helmholtz waves at Earth's dayside magnetopause. *Journal of Geophysical Research: Space Physics*, *120*, 5560–5573. https://doi.org/10.1002/2015ja021014

Welling, D. T., André, M., Dandouras, I., Delcourt, D., Fazakerley, A., Fontaine, D., et al. (2015). The Earth: Plasma sources, losses, and transport processes. *Space Science Reviews*, *192*(1–4), 145–208. https://doi.org/10.1007/s11214-015-0187-2

Wing, S., Johnson, J. R., Newell, P. T., & Meng, C.-I. (2005). Dawn-dusk asymmetries, ion spectra, and sources in the northward interplanetary magnetic field plasma sheet. *Journal of Geophysical Research*, *110*, A08205. https://doi.org/10.1029/2005JA011086

Yan, G. Q., Mozer, F., Shen, C., Chen, T., Parks, G. K., Cai, C. L., & McFadden, J. P. (2014). Kelvin-Helmholtz vortices observed by THEMIS at the duskside of the magnetopause under southward IMF. *Geophysical Research Letters*, *41*, 4427–4434. https://doi.org/10.1002/2014GL060589

Yan, G. Q., Parks, G. K., Cai, C. L., Chen, T., McFadden, J. P., & Ren, Y. (2020). Plasma transport into the duskside of the magnetopause caused by the Kelvin-Helmholtz Vortices in response to the northward turning of the interplanetary magnetic field observed by THEMIS. *Annals in Geophysics*, *38*, 263–273. https://doi.org/10.5194/angeo-38-263-2020